Received: 15 April 2024 | Accepted: 29 June 2024

DOI: 10.1111/mice.13304

COMPUTER-AIDED CIVIL AND INFRASTRUCTURE ENGINEERING WILEY

RESEARCH ARTICLE

Multiresolution dynamic mode decomposition approach for wind pressure analysis and reconstruction around buildings

Reda Snaiki | **Seyedeh Fatemeh Mirfakhar**

Department of Construction Engineering, École de Technologie Supérieure, Université du Québec, Montréal, Québec, Canada

Correspondence
Reda Snaiki, Département de génie de la construction, École de technologie supérieure, Université du Québec, 1100, rue Notre-Dame Ouest, bureau A-1490, Montréal, Québec H3C 1K, Canada.
Email: Reda.Snaiki@etsmtl.ca

Funding information
Natural Sciences and Engineering Research Council of Canada (NSERC), Grant/Award Number: CRSNG RGPIN 2022-03492

Abstract

Accurate wind pressure analysis on high-rise buildings is critical for wind load prediction. However, traditional methods struggle with the inherent complexity and multiscale nature of these data. Furthermore, the high cost and practical limitations of deploying extensive sensor networks restrict the data collection capabilities. This study addresses these limitations by introducing a novel framework for optimal sensor placement on high-rise buildings. The framework leverages the strengths of multiresolution dynamic mode decomposition (mrDMD) for feature extraction and incorporates a novel regularization term within an existing sensor placement algorithm under constraints. This innovative term enables the algorithm to consider real-world system constraints during sensor selection, leading to a more practical and efficient solution for wind pressure analysis. mrDMD effectively analyzes the multiscale features of wind pressure data. The extracted mrDMD modes, combined with the enhanced constrained QR decomposition technique, guide the selection of informative sensor locations. This approach minimizes the required number of sensors while ensuring accurate pressure field reconstruction and adhering to real-world placement constraints. The effectiveness of this method is validated using data from a scaled building model tested in a wind tunnel. This approach has the potential to revolutionize wind pressure analysis for high-rise buildings, paving the way for advancements in digital twins, real-time monitoring, and risk assessment of wind loads.

1 | INTRODUCTION

Tall and flexible buildings are particularly vulnerable to wind's dynamic forces, often leading to glass and facade damage (Chen & Kareem, 2004; Cui & Caracoglia, 2018; Hu et al., 2019; Huang & Chen, 2007). To ensure the structural integrity and functionality (serviceability) of these buildings (Kociecki & Adeli, 2014; Meena et al., 2022; Park & Adeli, 1997), the pressure distribution needs to be analyzed across their exterior surfaces. This information is also instrumental in devising optimal control and mitigation strategies (Aldwaik & Adeli, 2014; Gutierrez Soto & Adeli, 2017; Kim & Adeli, 2005; Wang & Adeli, 2015). While computational fluid dynamics offers a versatile tool for simulating pressure distributions across building surfaces (Bernardini et al., 2015; Wijesooriya et al., 2023),

wind tunnel testing remains the established benchmark for validation due to its ability to replicate real-world wind conditions (Tanaka et al., 2012; Whiteman et al., 2022). Wind tunnels allow for more accurate modeling of wind's impact on tall buildings and provide a tool for optimizing the building's aerodynamic performance. This optimization can involve modifying the building's shape to minimize wind pressure, with these changes being tested directly in the wind tunnel (Elshaer et al., 2017; S. Li et al., 2021; Sharma et al., 2018; Tse et al., 2009). Recent advancements in pressure transducer design, data acquisition systems, and data management have significantly improved the experimental analysis of wind forces on tall buildings. However, the analysis of wind pressure fields on tall buildings is hindered by their inherent randomness, high-dimensionality, noisy sensor data, and the wind's own fluctuating nature (Luo & Kareem, 2021). These factors make it difficult to analyze the pressure fields using traditional statistical methods like correlation or coherence functions (Carassale, 2012). In addition, the current measurement capabilities are limited, making it challenging to separate the various physical phenomena occurring at micro and macro scales within the pressure field. Accurately predicting the behavior of complex systems, like wind pressure on tall buildings, requires the ability to measure these multiscale phenomena across different scales. This improved understanding is essential to develop control measures that mitigate wind effects. On the other hand, sensor placement plays a central role in capturing the pressure field dynamics and estimating the full state of the system (Amezquita-Sanchez et al., 2018; Bai et al., 2017; Nair & Taira, 2015). However, the cost and limitations of deploying sensors, especially for real-time monitoring of actual high-rise buildings, pose a significant challenge. By strategically placing sensors (Yuan et al., 2023), valuable insights can be gained into the coherent structures within the pressure field. Optimizing sensor placement becomes critical to achieve accurate analysis while balancing cost constraints (Ma et al., 2023).

The exploration of random pressure fields and their impact on structures has been a topic of extensive research. Among various established techniques, proper orthogonal decomposition (POD) stands out as a powerful tool for analyzing spatiotemporally varying random wind pressure fields (e.g., Bastine et al., 2018; Carassale & Brunenghi, 2011; Chen & Kareem, 2005; Tamura et al., 1999). The core concept of POD lies in transforming the initial pressure data into a set of uncorrelated and orthogonal spatial modes. Importantly, POD ranks these modes based on their energy content, with the first mode capturing the most significant variations in the pressure field. Higher-order modes capture features with progressively lower energy, but these features can still contain valuable information. While POD offers valuable insights, it is essential to acknowledge its limitations. First, POD analysis focuses solely on the second-order statistics of the pressure field. Second, a single POD mode can encompass a combination of various frequencies within the pressure field, therefore information about the specific frequency content of the pressure field might be lost (Muld et al., 2012; Zhang et al., 2014; Zhao et al., 2019). For a more comprehensive understanding of pressure field dynamics, other techniques like dynamic mode decomposition (DMD) have been explored. Unlike variance-based methods like POD, DMD is an equation-free technique closely tied to the spectral analysis of the Koopman operator (Bevanda et al., 2021). In DMD, spatial features and their associated temporal characteristics are extracted from data while both temporal correlation and frequency information are preserved. This characteristic allows DMD to provide interpretable features directly associated with the system's dynamics, making it useful for constructing predictive models and comprehending complex physical processes. Extensive research has demonstrated the effectiveness of DMD in extracting flow structures and dynamic features across various flow types (Fu et al., 2023; C. Y. Li et al., 2022; Li et al., 2023; Luo & Kareem, 2021; Zhou et al., 2021). However, standard DMD struggles to approximate intermittent and transient phenomena with noise because the modes it obtains might not be enough to represent a broader range of dynamics (Benito et al., 2011; Hwang et al., 2023; Kutz et al., 2016). To address the limitations of standard DMD, a more advanced technique called multiresolution DMD (mrDMD) has been developed (Kutz et al., 2016). This technique demonstrates comparable performance to other advanced methods (Li et al., 2017; Perez-Ramirez et al., 2016). It utilizes a hierarchical temporal sampling framework similar to wavelet decomposition. This framework breaks down the data into a nested sequence of subspaces, each representing a specific timescale. Within each subspace, mrDMD uses the DMD algorithm to extract dominant dynamical modes, effectively capturing the system's characteristic evolution at that timescale. Through this recursive decomposition and analysis, mrDMD enables the characterization of complex phenomena governed by processes unfolding across different temporal scales.

Extracting meaningful data from wind tunnel tests or field measurements requires strategically placed sensors to capture the system's complete state. However, a critical challenge lies in determining the optimal number and location of these sensors. This is often constrained by two factors: (1) Uncertainty—where the exact number of sensors needed is often unknown beforehand; (2) cost—since the sensors can be expensive (Aldwaik & Adeli, 2014; Gao et al., 2024; Xie et al., 2022), making a

dense network financially impractical. For simple structures with well-defined geometries and few degrees of freedom, engineers can often rely on experience and intuition to place pressure taps strategically in wind tunnel tests, effectively gauging pressure distribution. However, for complex, large-scale structures, this approach becomes insufficient. Determining the optimal sensor layout for these structures remains a significant challenge (Jiang & Adeli, 2007; Meo & Zumpano, 2005; Papadimitriou, 2004; Tan & Zhang, 2020). While traditional optimization methods can be used to determine sensor locations, they can be computationally expensive. To address this, researchers have explored heuristic approaches like genetic algorithms and monkey algorithms (e.g., Liu et al., 2008; Yao et al., 1993; Yi et al., 2011). These techniques offer a faster path to solutions. However, there is a trade-off. Heuristic approaches rely on pre-defined hyperparameters that can significantly impact the final results. Choosing the optimal hyperparameters can be challenging, and these methods may not always guarantee the absolute best solution compared to traditional optimization techniques (Erichson et al., 2020; Manohar et al., 2018; Yang, 2021). In essence, these heuristic approaches offer a balance between speed and optimality. They can be a valuable tool for initial sensor placement, but further refinement might be needed using more rigorous optimization methods (Gao et al., 2023; Manohar et al., 2019) especially when constraints are involved (Karnik et al., 2024).

In this study, the mrDMD technique is implemented to separate complex wind-induced pressure dynamics into a hierarchy of components across different timescales. By leveraging a hierarchical sampling framework similar to wavelet decomposition, mrDMD addresses the challenges posed by noisy, transient, and multiscale systems, overcoming the limitations of standard DMD. Extracted mrDMD modes are then used to determine the optimal sensor placement while considering real-world system constraints. The study proposes a novel adaptation of a pivoted QR factorization technique (Drmač & Gugercin, 2016; Higham, 2000; Karnik et al., 2024; Manohar et al., 2018, 2022). This adaptation introduces a regularization term that builds upon the algorithm's existing constraints. This novel term offers several advantages: It penalizes overly complex solutions (promoting sparsity and informative sensor locations), prevents overfitting by mitigating noise, and reduces noise sensitivity in sensor placement decisions. Furthermore, the term can be tailored to incorporate additional real-world considerations, such as environmental factors. This innovative approach balances accurate pressure field reconstruction with minimal instrumentation, adhering to practical limitations while offering flexibility for diverse constraints. Due to the inherent trade-off between spatial and temporal resolution, the study investigates data augmentation approaches like time-delay embedding and interpolation to address limited spatial resolution and ensure effective sensor placement. The effectiveness of the proposed framework will be demonstrated through application to a scaled model of a high-rise building tested in a boundary layer wind tunnel.

2 | METHODOLOGY

DMD is a mathematical and data analysis technique used to extract dynamic patterns and spatiotemporal features from time-series data. Due to its simplicity and its ability to assist in understanding the behavior of complex dynamical systems, DMD has been widely applied to several applications including fluid dynamics, engineering, atmospheric science, and neuroscience. DMD allows for the approximation and understanding of the underlying dynamics of a system from observed data without requiring knowledge of the system's governing equations. It is closely connected to Koopman spectral theory (Lange et al., 2021) and can be seen as a finite-dimensional approximation to the Koopman operator, which is an infinite-dimensional linear operator used to represent the evolution of nonlinear dynamic systems. Specifically, DMD aims to extract the dominant dynamic modes and eigenvalues from time-series data. It provides a practical and computationally efficient way to approximate the Koopman operator by projecting the data onto a finite-dimensional subspace spanned by DMD modes. DMD essentially linearizes the system's dynamic, making it more accessible for analysis.

Let $\boldsymbol{x_i} \in \mathbb{R}^n$ be a column vector containing n data points at a time t_i and corresponding to the ith snapshot matrix. Assuming that m snapshots of data are available, they can be arranged into two data matrices as follows:

$$\boldsymbol{X} = [\boldsymbol{x}_1, \boldsymbol{x}_2, ..., \boldsymbol{x}_{m-1}] \text{ and } \boldsymbol{X'} = [\boldsymbol{x}_2, \boldsymbol{x}_3, ..., \boldsymbol{x}_m] \quad (1)$$

In this case, regularly spaced sampling in time was considered (i.e., $t_{i+1} = t_i + \Delta t$). However, the algorithm can also be extended to allow for both sparse spatial (Brunton et al., 2016) and temporal (Tu et al., 2014) collection of data along with irregularly spaced collection times (Dawson et al., 2016; Hemati et al., 2017). In DMD, time snapshots of high-dimensional system states are used directly to construct a spatiotemporal decomposition. Specifically, DMD aims to find the best-fit linear operator $\boldsymbol{A} \in \mathbb{R}^{n,n}$ such that $\boldsymbol{X'} = \boldsymbol{AX}$ based on the least-squares minimization of the Frobenius norm (Kutz et al., 2016; Rowley et al., 2009; Schmid, 2010; Tu et al., 2014) of the error:

$$\boldsymbol{A} = \underset{\boldsymbol{A}}{\operatorname{argmin}} \|\boldsymbol{X'} - \boldsymbol{AX}\|_F = \boldsymbol{X'X}^{\dagger} \quad (2)$$

ALGORITHM 1 Pseudo-code for the DMD algorithm.

Input: Time-series data matrix containing m snapshots
Output: DMD modes $\boldsymbol{\phi} \in \mathbb{C}^{m\times r}$, eigenvalues $\boldsymbol{\Lambda} \in \mathbb{C}^{r\times r}$, and reconstructed dynamics $\boldsymbol{x}_{DMD}(t)$
1. Snapshot matrices
Construct two data matrices $\boldsymbol{X}$ and $\boldsymbol{X}'$ by shifting the original data matrix by one time step, where $\boldsymbol{X}'$ contains data from the next time step (Equation 1).
2. Singular value decomposition (SVD)
Perform SVD on matrix $\boldsymbol{X}$: $\boldsymbol{X} = \boldsymbol{U}\boldsymbol{\Sigma}\boldsymbol{V}^*$ where $\boldsymbol{U} \in \mathbb{C}^{n\times n}$, $\boldsymbol{\Sigma} \in \mathbb{C}^{n\times(m-1)}$, and $\boldsymbol{V}^* \in \mathbb{C}^{(m-1)\times(m-1)}$ are the left singular vectors, singular values, and conjugate transpose of the right singular vectors, respectively. The * denotes the complex conjugate transpose.
3. Truncated SVD
Truncate the SVD to retain the top r singular values and corresponding columns of $\boldsymbol{U}_r \in \mathbb{C}^{n\times r}$, $\boldsymbol{\Sigma}_r \in \mathbb{C}^{r\times r}$ and $\boldsymbol{V}_r^* \in \mathbb{C}^{r\times(m-1)}$
4. Dynamics matrix approximation
Construct the matrix $\tilde{\boldsymbol{A}} = \boldsymbol{U}_r^* \boldsymbol{X}'\boldsymbol{V}_r\boldsymbol{\Sigma}_r^{-1}$ with $\tilde{\boldsymbol{A}} \in \mathbb{C}^{r\times r}$
5. Eigen decomposition of $\tilde{A}$
Perform the Eigen decomposition of $\tilde{\boldsymbol{A}}$ to obtain the eigenvectors $\boldsymbol{W}$ and eigenvalues $\boldsymbol{\Lambda}$ with elements λ_k: $\tilde{\boldsymbol{A}}\boldsymbol{W} = \boldsymbol{W}\boldsymbol{\Lambda}$
6. Computation of DMD Modes
Compute a DMD mode matrix whose columns are the eigenvectors $\boldsymbol{\phi}_k$ as: $\boldsymbol{\phi} = \boldsymbol{X}'\boldsymbol{V}_r\boldsymbol{\Sigma}_r^{-1}\boldsymbol{W}$
7. Reconstructed dynamics
Reconstruct the dynamics at any time t using the DMD model: $\boldsymbol{x}_{DMD}(t) = \sum_{j=1}^{r} b_k(0)\boldsymbol{\phi}_k \exp(\omega_k t) = \boldsymbol{\phi}\,\mathrm{diag}(\exp(\omega t))\boldsymbol{b}$ with $b_k(0)$ is the initial amplitude of each mode, $\boldsymbol{b}$ is a vector of the coefficients b_k given as $\boldsymbol{b} = \phi^{\dagger}\boldsymbol{x}_1$, $\omega_k = \ln(\lambda_k)/\Delta t$ and Δt time step between consecutive snapshots.

where $\|.\|_F$ = Frobenius norm; and † is the Moore–Penrose pseudoinverse. Hence, DMD fits a linear approximation $\boldsymbol{A}$ by using a pseudoinverse operation without explicitly computing $\boldsymbol{A}$. The pseudocode of the DMD technique is presented in Algorithm 1.

It should be noted that DMD approximation as detailed in Algorithm 1 introduces systematic bias in the eigenvalue computation of noisy data (Dawson et al., 2016; Hemati et al., 2017). To correct for this, a weighted approximation of $\boldsymbol{A}$ is constructed and used in this study that incorporates both forward ($\boldsymbol{X}' = \boldsymbol{A}_f\boldsymbol{X}$) and backward ($\boldsymbol{X} = \boldsymbol{A}_b\boldsymbol{X}'$) time evolution (Dawson et al., 2016) such that $\boldsymbol{A} = (\boldsymbol{A}_f\boldsymbol{A}_b^{-1})^{1/2}$. Despite its widespread success in various applications, DMD often struggles to approximate intermittent and transient phenomena (Kutz et al., 2016).

2.1 | mrDMD

The mrDMD is an algorithm that addresses the inherent limitation of standard DMD in handling data exhibiting multiscale dynamics. It leverages a hierarchical temporal sampling framework analogous to wavelet decomposition as illustrated in Figure 1. This framework decomposes the data into a nested sequence of subspaces, each corresponding to a specific timescale. Within each subspace, mrDMD employs the DMD algorithm to extract the dominant dynamical modes, effectively capturing the characteristic evolution of the system at that particular timescale. Through this recursive decomposition and analysis that continues until a desired or prescribed decomposition level has been achieved, mrDMD facilitates the characterization of complex phenomena governed by processes unfolding across disparate temporal scales.

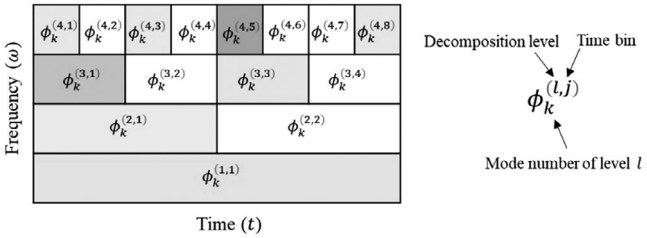

FIGURE 1 Schematic representation of the multiresolution dynamic mode decomposition (mrDMD) procedure.

mrDMD employs an iterative decomposition strategy to capture multiscale dynamics. In the first iteration, it analyzes the entire data sequence, represented by the largest sampling window. The DMD algorithm is then applied to extract the dominant low-frequency modes, which capture the slow-evolving features of the system. These modes are subsequently separated from the data, leaving a residual containing the higher-frequency components. Subsequent iterations progressively refine the analysis by halving the sampling window size. Within each window, DMD again identifies and extracts the slow modes. This recursive process isolates dynamical behavior across a range of timescales until a desired or prescribed decomposition level has been achieved. The final residual signal incorporates the fastest dynamics, characterized by a time resolution determined by the number of iterations. The mrDMD solution expansion can be expressed as

$$x_{mrDMD}(t) = \sum_{l=1}^{L}\sum_{j=1}^{J}\sum_{k=1}^{m_L} f_{l,j}(t)\, b_k^{(l,j)}\phi_k^{(l,j)}\exp\left(\omega_k^{(l,j)}t\right) \tag{3}$$

where L is number of decomposition levels; J is the number of time bins per level ($J = 2^{(l-1)}$); m_L is the number of modes extracted at each level. The indicator function

$f_{l,j}(t)$ is typically defined as

$$f_{l,j}(t) = \begin{cases} 1, & t \in \left[t_j^l, t_{j+1}^l\right] \\ 0, & \text{elsewhere} \end{cases} \quad \text{with } j = 1,\ 2,\ \ldots,\ 2^{(l-1)} \tag{4}$$

where $t_j^l, t_{j+1}^l \in \mathbb{R}^+$ determine the interval of the jth time bin at the lth decomposition level. This function is only nonzero in the interval, or time bin, associated with the value j. However, since the sampling bin has a hard cut-off, it might introduce artificial high-frequency oscillations. To address this, one could consider using wavelet functions for the sifting operation. This would allow the time function $f_{l,j}(t)$ to be represented by various wavelet bases, such as Haar (Haar, 1910), Daubechies (Waqas et al., 2020), and Mexican Hat (Lindeberg, 2015), among others. In this study, a Haar-like windowing in time is employed due to its simplicity and efficiency.

2.2 | Optimal sensor placement

This study introduces an advanced framework for analyzing and predicting multiscale dynamical systems by employing a combination of mrDMD and spatial sampling while incorporating system constraints. Although localized time-frequency analysis offers a powerful tool for studying such systems, it presents a significant hurdle for future state prediction. This challenge arises because the dominant modes within a new time window are unknown a priori. To overcome this limitation, the study incorporates additional information in the form of real-time state observations or sensor measurements. By leveraging these data, the problem of future state prediction can be reformulated as the reconstruction of high-dimensional states from the acquired observations. This essentially translates to estimating the appropriate temporal coefficients within the library of modes obtained through mrDMD. The discussion begins by examining the unconstrained case of the pivoted QR decomposition technique. Subsequently, the discussion will focus on the constrained QR decomposition technique.

Based on the mrDMD procedure, a library of dynamical modes can be obtained which can be represented as

$$\boldsymbol{\Phi} = \left[\phi_k^{(1,1)}\ \phi_k^{(2,1)}\ \phi_k^{(2,2)}\ \phi_k^{(3,1)} \ldots\ \phi_k^{(3,4)} \ldots\ \phi_k^{(l,j)} \ldots\right] \tag{5}$$

For a given (l, j), $\phi_k^{(l,j)}$ might include more than one mode. Therefore, the state $\boldsymbol{x}(t)$ can be approximated using a linear combination of the columns of $\boldsymbol{\Phi}$ leading to $\boldsymbol{x}(t) = \boldsymbol{\Phi a}(t)$ where $\boldsymbol{a}(t)$ represents the time-dependent coefficients. Predicting future states poses a challenge in identifying the active components of $\boldsymbol{a}(t)$ at a given time. This difficulty stems from the fact that mrDMD modes are localized in the time-frequency domain and do not enforce globally periodic temporal behavior. The information required for state estimation can often be obtained from point observations of the underlying state vector. These observations can be conveniently represented as a vector, denoted by $\boldsymbol{y} \in \mathbb{R}^p$ $(p \ll n)$. A key assumption in this approach is the existence of a linear relationship between $\boldsymbol{y}$ and the time-dependent coefficients which can be expressed as

$$\boldsymbol{y} = \boldsymbol{Cx} + \boldsymbol{\eta} = \boldsymbol{C\Phi a} + \boldsymbol{\eta} \tag{6}$$

where $\boldsymbol{C} \in \mathbb{R}^{p \times n}$ is the measurement matrix; and $\boldsymbol{\eta}$ is the additive white noise. The high-dimensional states can be directly recovered from measurements using the maximum likelihood estimate of the basis coefficients, $\hat{\boldsymbol{a}} = \left(\boldsymbol{C\Phi}_r\right)^{\dagger} \boldsymbol{y}$:

$$\hat{\boldsymbol{x}} = \boldsymbol{\Phi}_r \left(\boldsymbol{C\Phi}_r\right)^{\dagger} \boldsymbol{y} \tag{7}$$

where $\boldsymbol{\Phi}_r$ is the identified mrDMD modes whose amplitudes exceed a given threshold ε such that $r := \{i \in [1, \ldots, r] \mid |b_i| \rangle \varepsilon\}$. It should be noted that the strategic selection of sensor measurements allows for an extremely small number of deployed sensors to be used. The optimal solution to this problem involves placing sensors at limited points in the domain to reconstruct the pressure field over the entire domain accurately. Therefore, the design of experiments aims to optimize the sensor selection $\boldsymbol{C}$ to optimize statistics of the estimation error $\boldsymbol{a} - \hat{\boldsymbol{a}}$ by minimizing some scalar measure of the "size" of the error covariance:

$$\boldsymbol{\Sigma} = \mathrm{Var}\left(\boldsymbol{a} - \hat{\boldsymbol{a}}\right) = \sigma^2 \left[\left(\boldsymbol{C\Phi}_r\right)^T \left(\boldsymbol{C\Phi}_r\right)\right]^{-1} \tag{8}$$

The optimal design criterion for sensor placement is expressed as (Candes & Wakin, 2008; Candès et al., 2006)

$$\gamma_* = \underset{\boldsymbol{C}}{\mathrm{argmax}} \log\det \left[\left(\boldsymbol{C\Phi}_r\right)^T \left(\boldsymbol{C\Phi}_r\right)\right] \tag{9}$$

The measurement matrix $\boldsymbol{C}$ is further assumed to encode point measurements with unit entries in a sparse matrix such that:

$$\boldsymbol{C} = \left[\boldsymbol{e}_{\gamma_1}\ \boldsymbol{e}_{\gamma_2}\ \ldots\ \boldsymbol{e}_{\gamma_p}\right]^T \tag{10}$$

where $\gamma = \{\gamma_1, \gamma_2, \ldots, \gamma_p\} \subset \{1, 2, \ldots, n\}$ denotes the index set of sensor locations with cardinality p; $\boldsymbol{e}_{\gamma j}$ is the canonical basis vector with a unit entry in the component j (where a sensor should be placed) and zeros elsewhere.

In this study, an efficient and greedy strategy for optimizing sensor selection (Equation 9) is used, which is based on the pivoted QR factorization technique (Drmač & Gugercin, 2016; Manohar et al., 2018, 2022). The QR factorization with column pivoting decomposes a matrix $\boldsymbol{A} \in \mathbb{R}^{m\times n}$ into a product of an orthogonal matrix $\boldsymbol{Q}$ (or a unitary matrix in the case of complex matrices) and an upper right triangular matrix $\boldsymbol{R}$, such that $\boldsymbol{AC^T} = \boldsymbol{QR}$, where $\boldsymbol{C}$ a column permutation matrix. With the QR factorization applied to $\boldsymbol{\Phi_r^T}$, the following determinant can be simplified as

$$\left|\det \boldsymbol{\Phi}_r^T \boldsymbol{C}^T\right| = |\det \boldsymbol{Q}|\,|\det \boldsymbol{R}| = \prod_i |\boldsymbol{R}_{ii}| \tag{11}$$

This results in the following diagonal dominance structure in $\boldsymbol{R}$:

$$|\boldsymbol{R}_{ii}|^2 \geq \sum_{j=i}^{k} \left|\boldsymbol{R}_{jk}\right|^2,\ 1 \leq i \leq k \leq r \tag{12}$$

where $\boldsymbol{R}_{ii}$ is the diagonal entries in the upper-triangular matrix $\boldsymbol{R}$. Using the results of Equation (11), the $\log\det[(\boldsymbol{C\Phi}_r)^T(\boldsymbol{C\Phi}_r)]$ can be simply expressed as

$$\log\det\left[(\boldsymbol{C\Phi}_r)^T(\boldsymbol{C\Phi}_r)\right] = \log\left(\prod_{i=1}^{r}\boldsymbol{R}_{ii}^2\right) = \log\boldsymbol{R}_{11}^2 + \log\boldsymbol{R}_{22}^2 + \cdots + \log\boldsymbol{R}_{rr}^2 \tag{13}$$

With this approach, p point measurement indices (pivots) are generated that best characterize the dominant dynamical modes $\boldsymbol{\Phi}_r$. Although the minimal allowable number of sensors $p = r$ can be considered, additional sensors can be added for redundancy and robustness through oversampling optimization (Peherstorfer et al., 2020). The pseudocode of the QR pivoting without constraints is presented in Algorithm 2.

To accommodate the imposed system constraints, the optimal design criterion for sensor placement is revised as follows:

$$\gamma_* = \underset{\gamma,|\gamma|=p}{\operatorname{argmax}} \log\det\left[(\boldsymbol{C\Phi}_r)^T(\boldsymbol{C\Phi}_r)\right] - \lambda Rg(\gamma) \tag{14}$$

where $Rg(.)$ is the regularization function; and λ is the tuning parameter that controls the strength of the regularization. The pivoting procedure yields the following decomposition at the kth iteration:

$$\boldsymbol{\Phi}_r^{\mathrm{T}}\boldsymbol{P} = \boldsymbol{QR} = \boldsymbol{Q}\begin{bmatrix}\boldsymbol{R}_{11}^{(k)} & \boldsymbol{R}_{12}^{(k)}\\ \boldsymbol{0} & \boldsymbol{R}_{22}^{(k)}\end{bmatrix} \tag{15}$$

ALGORITHM 2 Pseudo-algorithm for the QR pivoting without cost constraints

Input: Dominant mrDMD modes $\boldsymbol{\Phi}_r^{\mathrm{T}}$

Output: Sensor indices ($\boldsymbol{\gamma}$)

1. **Procedure** QR Pivoting ($\boldsymbol{\Phi}_r^{\mathrm{T}}, p$)
2. $\gamma \leftarrow []$
3. **for** $k = 1, \ldots, p$ **do**
4. $\gamma_k = \operatorname{argmax}_{j\notin\gamma} \|a_j\|_2$
5. Find Householder $\tilde{\boldsymbol{Q}}$ such that $\tilde{\boldsymbol{Q}}.\begin{bmatrix}a_{kk}\\ .\\ .\\ .\\ a_{nk}\end{bmatrix} = \begin{bmatrix}\boldsymbol{R}_{nz}\\ 0\\ .\\ .\\ 0\end{bmatrix}$
   where $\boldsymbol{R}_{nz}$ represent nonzero diagonal entries in $\boldsymbol{R}$.
6. $\boldsymbol{\Phi}_r^{\mathrm{T}} \leftarrow \mathrm{diag}(\boldsymbol{I}_{k-1}, \tilde{\boldsymbol{Q}}).\boldsymbol{\Phi}_r^{\mathrm{T}}$
7. $\boldsymbol{\gamma} \leftarrow [\boldsymbol{\gamma}, \gamma_k]$
8. **end for**
9. **return** $\boldsymbol{\gamma}$
10. **end procedure**

where $\boldsymbol{R}_{11}^{(k)} \in \mathbb{R}^{k\times k}$ is an upper triangular matrix, $\boldsymbol{R}_{12}^{(k)} \in \mathbb{R}^{k\times(n-k)}$, $\boldsymbol{R}_{22}^{(k)} \in \mathbb{R}^{(m-k)\times(n-k)}$, and $\boldsymbol{P} \in \mathbb{R}^{n\times n}$ is a permutation matrix that encodes information about the first k-selected sensors. As established in the unconstrained QR decomposition with pivoting, the $(k+1)$th iteration selects a column from the submatrix $\boldsymbol{R}_{22}^{(k)}$ with the maximum norm. This column is then swapped with the $(k+1)$th column and the permutation indices are updated accordingly ($l = \underset{i=1,\ldots,n-k}{\operatorname{argmax}} \|r_{22_{(i)}}^{(k)}\|_2$). To incorporate system constraints and the regularization term (introduced in Equation 14) into the QR decomposition with pivoting, the column selection process is modified (Karnik et al., 2024). Unlike the unconstrained case where the column with the maximum two-norm from $\boldsymbol{R}_{22}^{(k)}$ is chosen, the constrained scenario restricts the selection to a subset of allowable indices that adhere to the imposed limitations. This ensures the chosen column satisfies the constraints while still prioritizing columns with large two-norms. Furthermore, by restricting the selection process in the final $r - s$ steps of pivoting (with s representing the indices allowed in the constrained region or total predetermined sensors), this method keeps the largest contributing terms in the objective function expansion from being significantly affected. Therefore, Equation (13) for the constrained case becomes:

$$\log\det\left[(\boldsymbol{C\Phi}_r)^T(\boldsymbol{C\Phi}_r)\right] - \lambda Rg(\gamma) = \log\left(\prod_{i=1}^{r}\boldsymbol{R}_{ii}^2\right)$$
$$-\lambda Rg(\gamma) = \log\boldsymbol{R}_{11}^2 + \log\boldsymbol{R}_{22}^2 + \cdots + \log\boldsymbol{R}_{(r-s)(r-s)}^2 + \cdots + \log\boldsymbol{R}_{rr}^2 - \lambda Rg(\gamma) \tag{16}$$

The introduction of constraints within the QR pivoting procedure depends on the specific type of constraint being enforced (Karnik et al., 2024). The core principle is to prioritize maximizing the leading diagonal entries of the $\boldsymbol{R}$ matrix during initial iterations. This ensures the establishment of a strong diagonal dominance property, crucial for numerical stability and convergence. Domain-specific constraints are then incorporated in the later stages (final $r - s$ steps) to optimize the trailing sub-diagonal entries ($\boldsymbol{R}_{ii}$). By restricting pivot selection to allowable locations that satisfy the constraints, this approach ensures adherence to domain limitations without significantly impacting the diagonal dominance property established earlier. This study explores two primary constraint scenarios within the QR pivoting framework.

The first scenario is "region-constrained" where either a maximum of s sensors or exactly s sensors are required in a designated region or set of regions. The remaining $r - s$ sensors must be placed outside the constrained region. If the maximum of s sensors is requested, the number of sensors in the constrained region should not exceed s. In this case, a pivot column is selected from the set of all columns until s pivots are in the constrained region. Subsequent pivots are chosen from the remaining unconstrained columns, maximizing their two-norms as well. If exactly s sensors are required within the constrained region, the algorithm follows the same procedure as the maximum placement scenario as long as the current number of sensors in the region is already s or more. However, if there are fewer than s sensors in the constrained region, the algorithm forces the placement of the remaining sensors in the constrained region at the end of the pivoting process. The second scenario considered is the "predetermined case," where certain sensor locations are already specified, and the goal is to optimize the locations of the remaining sensors. Here, the algorithm prioritizes selecting pivots (sensor locations) from all columns in $\boldsymbol{R}_{22}^{(k)}$ during the first $r - s$ iterations. Subsequently, during the final s iterations, the algorithm enforces the selection of the remaining user-specified sensor locations.

Incorporating a regularization term (Rg) into the cost function for QR decomposition with pivoting enhances sensor selection by mitigating overfitting and noise sensitivity. It also prevents the selection of highly correlated sensors that capture redundant information from specific locations. By penalizing configurations where chosen sensors have similar measurements (e.g., $Rg = \sum_{i \neq j} \rho_{\gamma_i, \gamma_j}$), the regularization term promotes diversity in sensor selection, ensuring that sensors capture information from different aspects of the system. The regularization term can also be designed to penalize configurations where sensors are clustered together or to ensure sensors are placed at a minimum distance from each other (e.g., $Rg = \sum_{i \neq j} \max(0, d_{\min} - d_{\gamma_i, \gamma_j})$) to ensure adequate coverage. Additionally, the regularization function can be tailored to consider environmental factors such as temperature, humidity, and terrain, which may affect sensor performance. This can be modeled by weighting sensor placement based on these factors, where the weighting factor can take the form: $\sum_i \omega_i f_i$ where ω_i is the weight and f_i is the environmental factor at sensor location i. By minimizing the total cost function, the QR decomposition with pivoting not only aims to minimize reconstruction error but also takes into account the regularization term, ensuring a more robust and diverse sensor placement.

3 | CASE STUDY

This section investigates the application of mrDMD to a case study. Subsequently, the potential for combining mrDMD with pivoted QR factorization while considering the system constraints for optimal pressure tap placement is explored. To augment the dimensionality of the available data for analysis, two data augmentation approaches, namely, time-delay embedding and interpolation, are examined.

3.1 | Wind tunnel experimental data

The wind pressure data for the selected high-rise building geometry were obtained from the Tokyo Polytechnic University aerodynamic database. The data were derived from tests conducted in an open-circuit wind tunnel with a test section measuring 1.2 × 1.0 m. A scaled model (1/400) of the high-rise building with dimensions 0.5 × 0.1 × 0.1 m (height × breadth × depth), was exposed to a simulated approach flow profile defined by a power-law wind profile with an exponent of 1/4. The mean wind speed at the top of the scaled building was fixed at 11 m/s with a turbulence intensity corresponding to category III (suburban terrain). For pressure measurements, the scaled model was equipped with a total of 500 pressure taps, evenly distributed across all surfaces, resulting in a sensor density of 125 taps per surface, as illustrated in Figure 2. These taps were arranged in a grid pattern of 5 × 25, corresponding to the horizontal and vertical axes. The pressure data were collected at a sampling frequency of 1000 Hz, with a total recording duration of 32.768 s. Consistent with prior investigations that employed convergence analysis to identify an optimal number of snapshots for subsequent analysis (Luo & Kareem, 2021; Zhou et al., 2021), the present study utilized the initial 2000 snapshots from the dataset. This

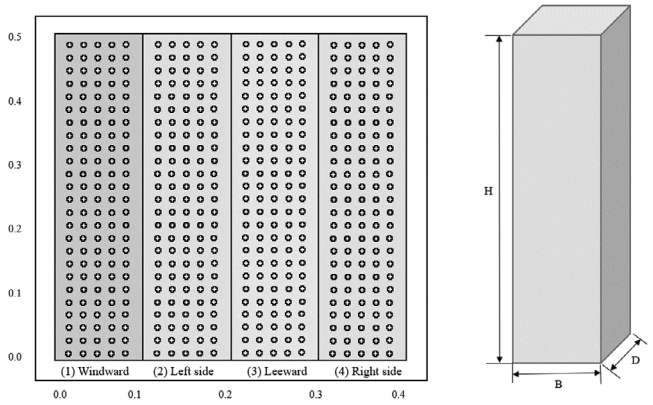

FIGURE 2 Schematic representation of the scaled building model, highlighting the distribution of pressure taps for wind tunnel testing.

selection strategy aligns with the established practice of identifying a truncation point that balances the capture of dominant dynamic modes with computational efficiency.

3.2 | mrDMD with time-delay embedding

3.2.1 | Time delay-embedding

Due to the significantly lower spatial resolution, compared to temporal resolution in the pressure field data, time-delay embedding (Brunton et al., 2017; Takens, 1981; Zhou et al., 2021) is employed in this section. This technique mitigates data distortion caused by noise and augments the spatial details within the input matrix. The accuracy of DMD results is highly sensitive to the selected embedding dimensions. In this case study, the spatial dimensionality is directly related to the number of pressure measurement points. Specifically, a Hankel matrix is constructed by arranging the elements of time-delayed coordinates (Frame & Towne, 2023) in a stacked manner such that:

$$\boldsymbol{X}_{aug} = [\boldsymbol{X}_1\boldsymbol{X}_2\cdots\boldsymbol{X}_{m-d+1}] = \begin{bmatrix} x_1 & x_2 & \cdots & x_{m-d+1} \\ x_2 & x_3 & \ddots & x_{m-d+2} \\ \vdots & \vdots & & \vdots \\ x_d & x_{d+1} & \cdots & x_m \end{bmatrix} \tag{17}$$

where d is the embedding number. Consequently, a pair of matrixes $\boldsymbol{X} = [\boldsymbol{X}_1\boldsymbol{X}_2...\boldsymbol{X}_{m-d}]$ and $\boldsymbol{X}' = [\boldsymbol{X}_2...\boldsymbol{X}_{m-d+1}]$ can be defined, and the DMD technique can be applied. Figure 3 compares the distribution of DMD eigenvalues within the real-imaginary plane for different embedding dimensions. The eigenvalues located outside the unit circle (i.e., the complex modulus is greater than 1)

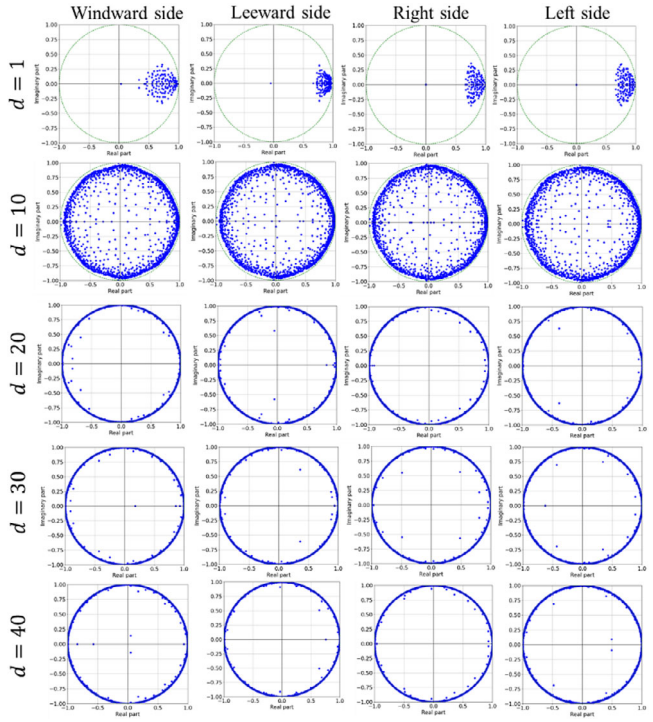

FIGURE 3 Distribution of DMD eigenvalues on the real-imaginary circle with different embedding numbers.

represent unstable states. Conversely, eigenvalues positioned on or near the circle's perimeter signify stable or neutrally stable modes. Points located inside the circle correspond to decaying modes that will eventually vanish.

As can be concluded from Figure 3, as d increases, the number of modal points within the unit circle also grows. This can be attributed to the fact that a larger embedding dimension essentially expands the state space of the reconstructed system, allowing for the identification of a wider range of dynamic modes. When $d = 1$, the technique effectively reduces to standard DMD. This scenario (i.e., $d = 1$) results in a significant number of modal points falling away from the unit circle. This observation verifies the limitations of standard DMD in accurately capturing the dynamics of high-dimensional, nonlinear systems, particularly when dealing with noisy data. On the other hand, when the embedding dimension reaches $d = 30$, Figure 3 demonstrates a substantial shift, with nearly all modal points located either on or very close to the unit circle. This signifies that a sufficient level of information has been captured to accurately represent the system dynamics. Further increases in the embedding dimension ($d > 30$) exhibit minimal impact on the distribution of modal eigenvalues, suggesting that a value of $d = 30$ provides an optimal balance between capturing essential dynamics and computational efficiency.

3.2.2 | mrDMD application

In this section, the mrDMD technique is employed to analyze the pressure signals acquired from the selected building geometry. The decomposition process involves a hierarchical approach with five levels. At each level, the slow spatiotemporal modes are extracted and only the dominant modes with the highest amplitudes are retained. Figure 4a visualizes the resulting modal amplitude maps for the windward and leeward faces within the time-frequency domain (a similar decomposition was performed for the right and left sides, but the results are omitted for brevity). Each bin within the figures is colored according to the average modal amplitude of the corresponding dynamics. It should be noted that Figure 4a employs normalized frequency, defined as $f_n = fH/V$, where f is the frequency, H is the building height, and V is the incoming wind speed. The selection of decomposition levels in mrDMD depends on the data's frequency content. Cut-off frequency, which separates information captured at different levels, is determined by two factors: the analyzed data's timespan within each level (inherent to the decomposition process) and an adjustable parameter called max_*cycle*. This parameter sets the overall frequency range for mrDMD analysis. In this study, the data's power spectral density (also shown in Figure 4b for two locations) was examined to identify its dominant frequencies. Based on this analysis, a value of 5 for max_*cycle* was chosen, ensuring that the decomposition captures the relevant frequency content of the pressure data ($f_n = 1.76$).

Figure 4a clearly reveals prominent modal signatures at specific decomposition levels. Lower levels capture slow-moving spatiotemporal dynamics, while higher levels (e.g., fifth level) reveal the fastest modes. Notably, the first decomposition levels effectively isolate the average pressure field over the entire 2-s time period. This demonstrates mrDMD's capability in accurately extracting the system's intrinsic modes. mrDMD offers a significant advantage by simultaneously visualizing dominant modes within a specific time-frequency range. This allows to focus on intervals with higher amplitudes that cannot be done with standard DMD unless appropriate sampling windows are pre-selected. Additionally, even with carefully selected windows in standard DMD, the previously extracted slow modes could contaminate the data at the level of interest. Therefore, mrDMD provides a principled algorithmic approach that facilitates data-driven discovery in complex systems. These identified modes directly contribute to the feature selection process, informing the formation of the index r ($r := \{i \in [1, \dots, r] \mid |b_i| \rangle \varepsilon\}$) used for sensor training. If higher frequency components are of interest, the number of decomposition levels can be simply increased. A more detailed analysis of the extracted modes will be presented in the subsequent sections.

3.2.3 | Pressure field reconstruction

To assess the reconstruction capability of mrDMD, the pressure field across all four building surfaces was reconstructed using the extracted high-energy modes obtained up to the fifth decomposition level. The root mean square error (RMSE) was employed to quantify the discrepancy between the reconstructed pressure coefficients and the observed data, defined over all time steps as follows:

$$\text{RMSE} = \sqrt{\frac{1}{mn}\sum_{j=1}^{m}\sum_{i=1}^{n}\left(P_{i,j}^{pred} - P_{i,j}^{obs}\right)^2} \tag{18}$$

where $P_{i,j}^{pred}$ is the predicted pressure coefficient; and $P_{i,j}^{obs}$ is the observed pressure coefficient. The mrDMD reconstruction achieved RMSE of 0.026, 0.038, 0.073, and 0.072 for the windward, leeward, right side, and left side, respectively; the corresponding mean percentage errors are 15.6%, 12%, 8.1% and 8%, respectively. The results demonstrate remarkably small RMSE values for the pressure field reconstructed using the five decomposition levels. This signifies the robustness of mrDMD's reconstruction capabilities, allowing for the reconstruction of any pressure field snapshot at any given time instant. The performance of the standard DMD procedure, on the other hand, was suboptimal, yielding higher RMSE values (e.g., 0.31 for the windward case). Figure 4c presents a comparison between the reconstruction and prediction results obtained by mrDMD with the actual point-wise pressure fluctuations measured on the windward face at three distinct time points ($t = 600\Delta t$, $t = 1000\Delta t$, and $t = 1600\Delta t$ with $\Delta t = 0.001$ s). Visual inspection of the results reveals a high degree of agreement between the wind pressure time series reconstructed by the mrDMD modes and the wind tunnel data. Furthermore, the corresponding RMSE values for these time instances were 0.030, 0.021, and 0.027, further supporting the accuracy of the mrDMD reconstruction.

Figure 4d illustrates the reconstruction of the spatial pressure distribution across the leeward face, right side, and left side of the building. Similar to the windward face, good agreement was achieved between the mrDMD results and the wind tunnel data. The corresponding RMSE values for the leeward face, right side, and left side were 0.018, 0.054, and 0.026, respectively. These results demonstrate the generalizability of mrDMD's reconstruction

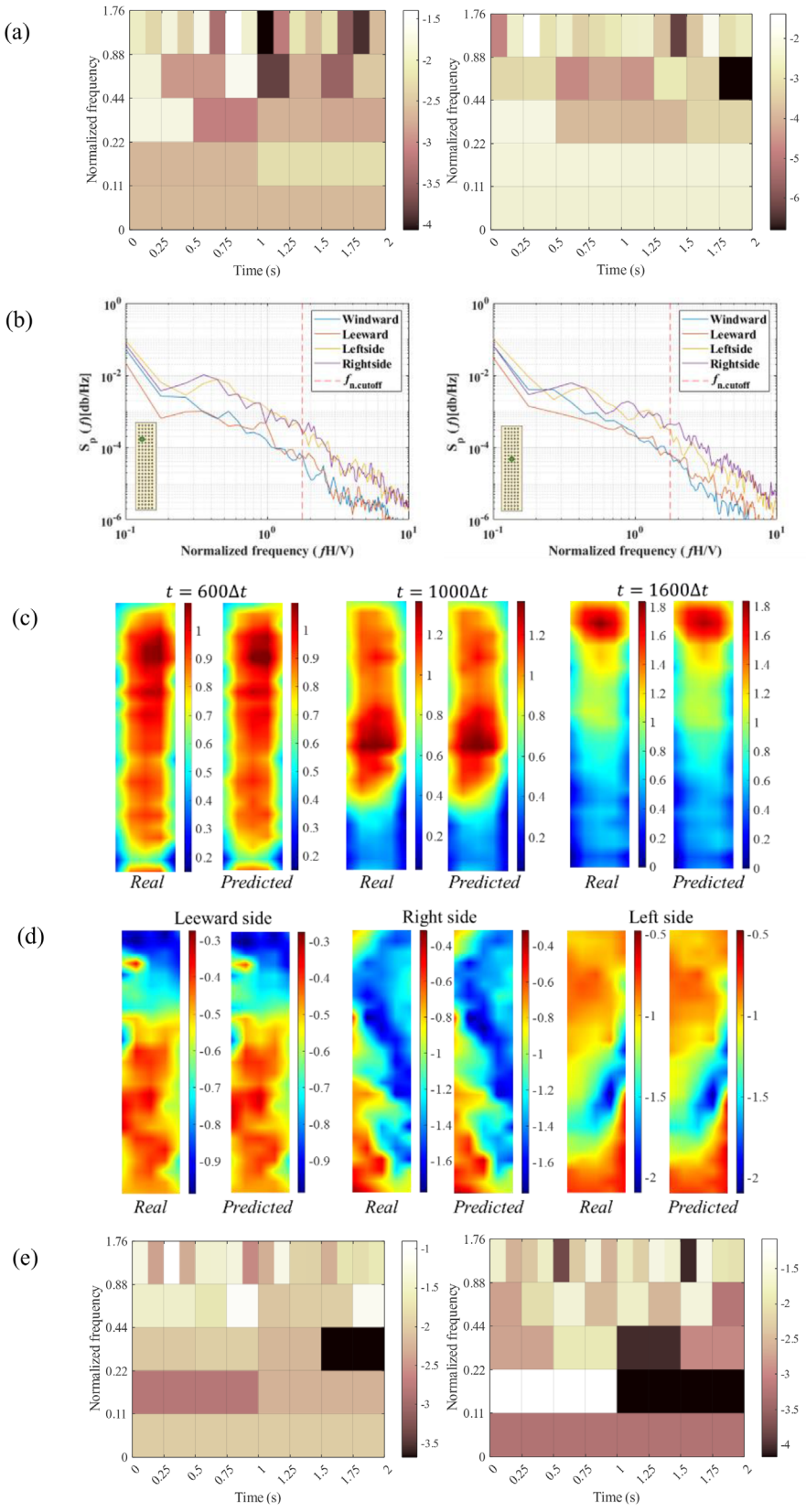

FIGURE 4 (a) mrDMD decomposition of the pressure fields for the windward (left) and leeward (right) surfaces using the time-embedding approach; (b) power spectral density of two randomly selected pressure points; (c) time-series reconstruction results of the windward face case at three-time instants using five decomposition levels with the time-embedding approach; (d) reconstruction of the pressure field across the leeward face, right side, and left side of the test object at $t = 1000\Delta t$ with the time-embedding approach; and (e) mrDMD decomposition of the pressure fields for the windward (left) and leeward (right) surfaces using the interpolation approach.

capabilities across various building surfaces. It is worth noting that the slightly higher RMSE values observed for the non-windward faces (leeward, right side, and left sides), compared to the windward face likely stem from two contributing factors. First, the flow patterns on these surfaces tend to be more complex than those on the windward face, potentially leading to higher discrepancies between the reconstructed and actual pressure fields. Second, the choice of using only five decomposition levels limited the captured normalized frequency range to up to 1.76 (as indicated in Figure 4a). High-frequency wind pressure fluctuations, if present, could contain significant modal information. Including these higher frequencies by increasing the decomposition levels might improve the reconstruction accuracy and lead to a closer match between the simulated and wind tunnel data. However, given the current results already demonstrate a good capability in reconstructing the pressure patterns, further refinement through additional decomposition levels may not be necessary for the present study.

3.3 | mrDMD with interpolation

3.3.1 | mrDMD application

This section revisits the application of mrDMD to the pressure signals. However, instead of utilizing the time-delay embedding technique to augment the data matrix, a simpler linear interpolation approach will be employed for augmentation. While more advanced interpolation methods like kriging (Van Beers & Kleijnen, 2004) exist, this study focuses on linear interpolation for simplicity. The mrDMD algorithm remains applicable to this alternative data augmentation strategy. The pressure sensor density is significantly increased, going from a grid of five taps by 25 taps on each facade (totaling 125 sensors) to a denser grid of 25 taps by 100 taps, resulting in 2500 data points. Figure 4e presents the resulting modal amplitude maps for the windward and leeward faces within the time-frequency domain.

While a direct comparison between the two mrDMD approaches (time-delay embedding vs. interpolation) is challenging due to the modification of the signal in the first approach, some general observations can be made regarding the modal signatures and features. Both approaches exhibit similar characteristics in certain aspects. Just like with time-delay embedding, the first decomposition levels obtained using interpolation effectively capture the average pressure field over the entire 2-s duration. Additionally, high-energy content is evident in the fifth level for both windward and leeward faces. For instance, for the leeward face, this high-energy region is particularly noticeable between $t = 1.5$ s and $t = 1.625$ s. The mrDMD reconstruction achieved RMSE of 0.015, 0.028, 0.045, and 0.049 for the windward, leeward, right side, and left side, respectively, and the corresponding mean percentage errors are 4.2%, 3.7%, 4.4%, and 4.6%, respectively. Figure 5a presents the reconstructed pressure distribution at a specific instant, $t = 1000\ \Delta t$. The RMSE between wind tunnel measurements and simulations for the windward face, leeward face, right side, and left side at $t = 1000\ \Delta t$ were 0.017, 0.018, 0.056, and 0.023, respectively. These low values indicate good agreement between the two methods.

3.3.2 | Analysis of DMD modes

In this study, the mrDMD capabilities in feature extraction for the pressure field will be prioritized along with its combination with an advanced sensor placement methodology rather than conducting a comprehensive analysis of the pressure field as seen in previous studies (e.g., Carassale, 2012; Luo & Kareem, 2021; Zhou et al., 2021). In general, it is acknowledged that the dominant factor influencing fluctuating aerodynamic loads on the building's windward face is the turbulence characteristics of the approaching flow. Furthermore, the aerodynamic loads experienced on the side and leeward faces exhibit a strong correlation with the dynamics of the wake region, particularly vortex shedding, which itself is influenced by the upstream flow turbulence. Extracting the intrinsic features of pressure distributions, particularly the high-frequency components associated with turbulence, presents a significant challenge for conventional DMD. This limitation arises from the inherent analysis approach of standard DMD, which operates by processing the entire pressure signal. This holistic analysis can lead to spectral leakage, where slower, dominant modes contaminate the faster modes containing the crucial turbulent signatures. Consequently, standard DMDs struggle to effectively isolate and capture the essential fast dynamics within the pressure field. In contrast, mrDMD overcomes this challenge by utilizing a sophisticated, hierarchical decomposition similar to wavelet analysis. This approach helps mrDMD sidestep the limitations of clustering methods, which can struggle with potentially contaminated modes from processing the entire signal. Consequently, mrDMD facilitates the isolation and analysis of important modes at various levels. This decomposition reveals a clear structure within the dynamics: Low-frequency, high-energy modes concentrated in the first levels (often termed "macroscale" modes) capture large-scale features. Conversely, high-frequency modes residing in the upper levels (often called "microscale" modes) represent small-scale turbulent eddies. In between these extremes, "mesoscale" modes can potentially be

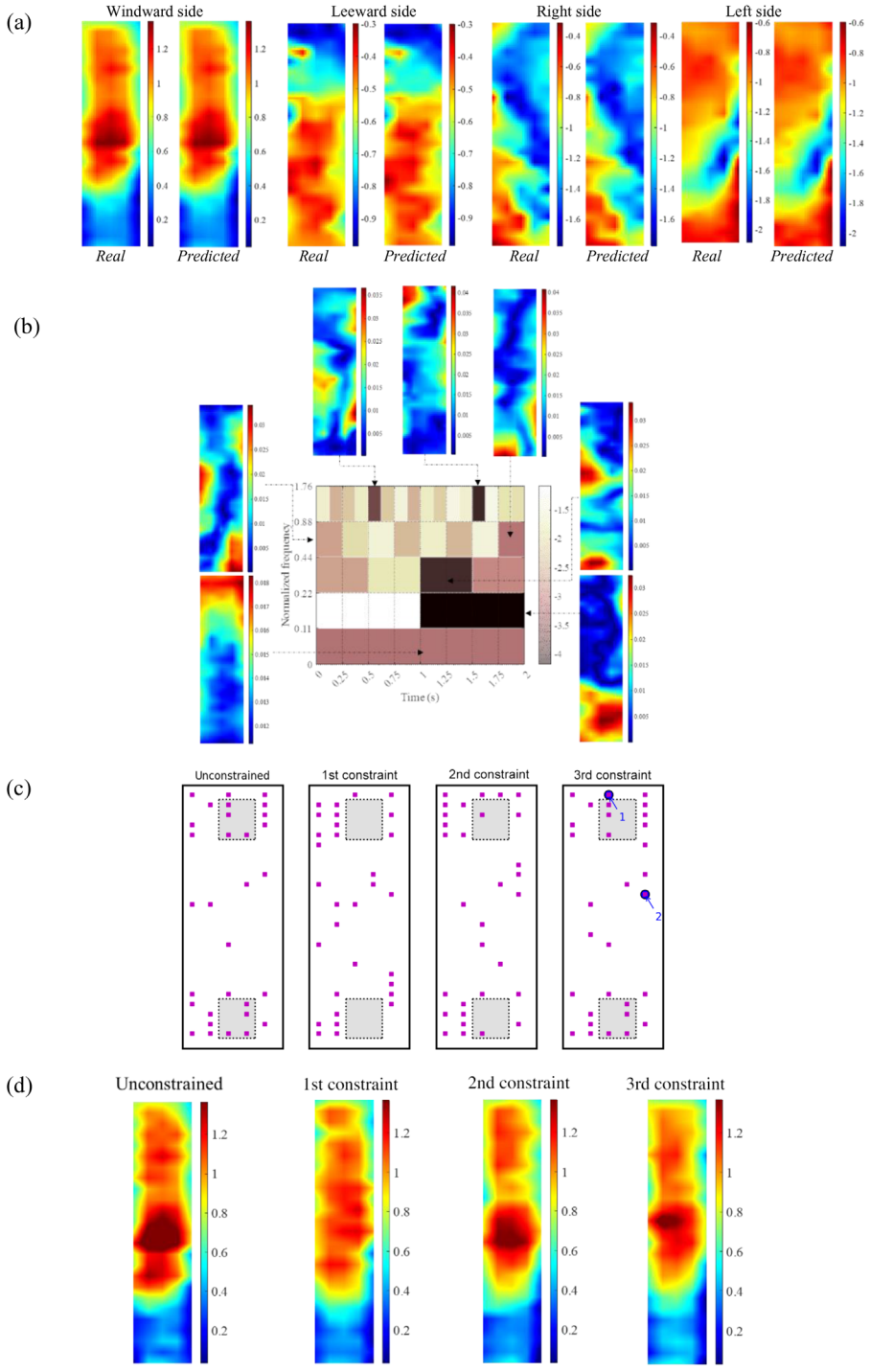

FIGURE 5 (a) Reconstruction of the pressure field across the windward face, leeward face, right side, and left side of the test object at $t = 1000\Delta t$; (b) visualization of the dominant modes identified using mrDMD at each decomposition level for the pressure distribution on the leeward face; (c) pressure sensor locations identified on the windward side of the building under several imposed constraints; and (d) reconstruction of the pressure field across the windward face at $t = 1000\Delta t$ under the selected constrained scenarios.

identified. The hierarchical decomposition of mrDMD unveils an energy cascade within the pressure fluctuations, mirroring the behavior observed in turbulence. This cascade resembles the energy transfer mechanisms in turbulence: energy injection, neutrally steady transfer, and eventual dissipation. Additionally, the spatial patterns observed in the pressure field exhibit a similarity to the distribution of eddy sizes (length scales) within the incoming turbulent flow. Figure 5b showcases some of the dominant modes extracted at different decomposition levels. These

modes visually depict the pressure fluctuations mimicking the turbulence cascade, with stages representing energy injection, transfer, and dissipation. The first decomposition level extracts large, low-frequency eddies with high energy. As the level increases, smaller, higher-frequency eddies become evident. This pressure pattern aligns with the distribution of eddy sizes (length scales) in the incoming turbulent flow. Notably, the spatial coherence within the extracted DMD modes progressively weakens from low levels (macroscale) to high levels (microscale). Including higher decomposition levels (beyond 1.76) would reveal even more distinct microscale eddies. Macroscale DMD effectively captures the global footprint of aerodynamic pressure, reflecting the overall distribution of fluctuating pressures acting on the model. Consequently, these macroscale modes can be directly linked to the energy injected by the incoming flow, representing its spatiotemporal characteristics. Microscale modes, on the other hand, represent the high-frequency, small-scale eddies. These eddies arise from instabilities due to local interactions between different fluid motions. Furthermore, the random distribution of peak values in most microscale DMD modes aligns with the inherent randomness and small size of these eddies. This randomness is further accentuated by the exponential decay observed in the mode amplitudes. This decay signifies the ultimate dissipation of kinetic energy carried by the small-scale turbulent motions.

3.4 | Optimal sensor placement

This section employs an advanced framework leveraging the mrDMD approach and pivoted QR factorization with constraints (detailed in Section 2.3) for the optimal placement of pressure taps in multiscale dynamical systems (Manohar et al., 2019). With this approach, p point measurement indices (pivots) are generated that best characterize the dominant dynamical modes $\mathbf{\Phi}_r$. It should be noted that this section will solely focus on the results obtained from the mrDMD approach applied to the interpolated wind pressure field. Notably, a similar approach can be extended to the time-embedding method. In addition, only the results for the windward case will provided as a similar approach can be applied to the other building faces (the results are omitted for brevity).

With a decomposition level (L) of 5, a total of 31 sensors were selected on the windward face. This number balances capturing the dominant mrDMD modes at this level with the overall decomposition complexity. Figure 5c illustrates the sensor locations for the unconstrained case. The corresponding RMSE between the reconstructed and observed pressure data at $t = 1000\Delta t$ is 0.079. In addition, the proposed sensor placement strategy can handle system constraints. Three scenarios are explored:

1. First constraint ("1st constraint"): No sensors in designated top and bottom regions (shaded in Figure 5c).
2. Second constraint ("2nd constraint"): Two sensors are required in designated regions (one per region), and the remaining 27 sensors are placed outside.
3. Third constraint ("3rd constraint"): Two predetermined sensors at specific locations (Figure 5c) are selected and the remaining sensor locations are optimized.

For each scenario, a regularization term is added to the QR decomposition cost function ($Rg = \sum_{i \neq j} \max(0, d_{\min} - d_{\gamma_i,\gamma_j})$). This term enforces a minimum distance between sensors ($d_{\min} = 0.02$ m) and penalizes configurations where sensors are too close. As discussed earlier (Section 2.3), this function can be tailored for various application needs.

The proposed algorithm demonstrates successful enforcement of the imposed constraints across all scenarios. This is reflected in the RMSE values for the reconstructed pressures at $t = 1000\Delta t$ (Figure 5d). These values are 0.107, 0.087, and 0.106 for the 1st, 2nd, and 3rd constraints, respectively. The sensor layout changes between configurations but preserves key locations (especially outside constrained regions), indicating their importance for capturing dominant features. Notably, the unconstrained and 3rd constrained layouts are very similar, with only two sensors replaced by the user-specified ones in the latter. It should be noted that reconstruction quality could be improved with more mrDMD modes. The final pressure sensor density is significantly increased from a 5×25 grid per facade (125 sensors) to a denser 25×100 grid (2500 sensors), comparable to numerical simulations. This density increase explains the performance difference, compared to using fewer sensors. While not shown here, the optimal sensor layout varies by building face due to the need for capturing different airflow patterns. More sensors are placed at corners and edges due to their increased aerodynamic complexity.

This sensor placement strategy leverages the QR algorithm to strategically position sensors that capture the essence of complex, multiscale phenomena by focusing on their dominant features. It further incorporates mrDMD to account for the varying temporal/frequency characteristics of the signal. By considering these multiscale aspects, this method significantly outperforms random sensor placement with the same number of sensors.

4 | DISCUSSION

This study presents an advanced framework for optimal sensor placement on building facades for wind pressure

analysis and prediction. The framework leverages the strengths of two key components:

- mrDMD analysis: This technique extracts the multiscale features of wind pressure data, capturing both dominant trends and higher-frequency variations.
- Constrained QR decomposition: This algorithm guides sensor selection while considering real-world constraints on sensor placement. It incorporates a regularization term to penalize undesired sensor configurations and utilizes the leading diagonal entries of the R matrix to prioritize informative sensor locations.

The mrDMD technique has been shown to outperform other established methods such as DMD and POD (e.g., Jolliffe & Cadima, 2016). For instance, considering an unconstrained scenario with full sensor access, the RMSE for the pressure field reconstruction on the windward side was significantly lower using mrDMD (0.015), compared to the POD technique (0.911).

The core analysis of this framework exhibits shape independence. As demonstrated in Equation (1), data are reorganized into a vector, making it independent of the specific building geometry. This allows for the extension of the method to various building shapes while maintaining the effectiveness of mrDMD in identifying relevant modes and the modified QR technique in finding optimal sensor locations. However, highly intricate geometries with complex details might require further investigation to ensure accurate sensor placement in such scenarios. The framework's adaptability extends beyond building shapes. The core methodology is designed to handle the complex, multi-scale nature of wind pressure observed in real-world scenarios. This includes the ability to accommodate non-steady-state wind conditions. By analyzing time-varying data with the mrDMD algorithm, the framework can capture transient wind pressure dynamics through pressure data collected over multiple time steps. Adjusting decomposition levels in mrDMD offers a balance between capturing high-frequency wind gusts and low-frequency pressure variations. Future validation with real-world building models under varying wind conditions will further solidify the framework's effectiveness in these practical situations.

As noted in Section 3, the choice of 2000 data snapshots was based on established convergence studies (e.g., Luo & Kareem, 2021) that determine the minimum amount of data needed for accurate mrDMD decomposition. This approach ensures sufficient information for capturing the underlying aerodynamic characteristics, including the dominant mean mode, quasi-periodic modes related to vortex shedding, and some transient effects, while avoiding unnecessary computational burden associated with using excessively large datasets. The wind tunnel data employed in this study captured these key features within the 2000 snapshots. However, the remaining data hold potential for future investigations that might explore higher-order transient dynamics.

It should be noted that this study employed an initial grid of sensors to facilitate the identification of mrDMD modes, a common approach for low-cost procedures like wind tunnel tests or numerical simulations. While this initial grid is not necessarily optimal, it provides a foundation for subsequent topology optimization using the extracted modes. However, the ultimate goal lies in the application for real cases where installing an initial grid on actual buildings is impractical and computationally expensive. This framework addresses this challenge by directly delivering the final, optimized sensor locations for installation on the building facade.

Furthermore, while the QR decomposition technique is generally efficient, exploring novel methods like convex relaxation (e.g., Błachowski et al., 2020; Joshi & Boyd, 2009) could be an interesting avenue for further improvement. This could potentially speed up the sensor selection process, making the framework even more attractive for real scenarios with massive datasets.

5 | CONCLUSION

This study successfully demonstrated the effectiveness of an advanced framework for wind pressure analysis and reconstruction on high-rise buildings. This framework combines the strengths of mrDMD and a constrained sensor placement strategy. mrDMD effectively addresses the limitations of standard DMD by characterizing the multiscale and transient dynamics of the wind pressure field. Notably, mrDMD's hierarchical decomposition revealed an energy cascade in pressure fluctuations reminiscent of the turbulence signature. This cascade reflects the transfer of energy within the flow (injection, transfer, dissipation). The decomposition process clearly distinguished low-frequency, energetic modes capturing large-scale features (macroscale) from high-frequency modes (microscale) representing small-scale eddies. Interestingly, the spatial patterns of the pressure field displayed a strong resemblance to the eddy size distribution observed in the incoming turbulent flow. The proposed framework facilitates the identification of an optimal sensor configuration for accurate pressure field reconstruction. With a decomposition level of 5, a total of 31 sensors were selected on the windward face, balancing the capture of dominant mrDMD modes with overall complexity. The corresponding RMSE between the reconstructed and observed pressure data at $t = 1000\Delta t$ was 0.079 for the unconstrained case. The framework effectively handles diverse

system constraints through a novel sensor placement strategy as demonstrated by achieving good reconstruction accuracy (RMSE values between 0.087 and 0.107) even when limited sensor placement options are available. In all cases, a regularization term was incorporated into the QR decomposition cost function to enforce a minimum distance between sensors and penalize overly dense configurations, ensuring practical implementation. This function can also be tailored to various application needs. Overall, this approach paves the way for a more efficient and cost-effective approach to structural health monitoring and wind load analysis in high-rise buildings, ultimately improving the safety and resilience of these structures.

ACKNOWLEDGMENTS

This work was supported by the Natural Sciences and Engineering Research Council of Canada (NSERC) [Grant Number CRSNG RGPIN 2022-03492].

REFERENCES

Aldwaik, M., & Adeli, H. (2014). Advances in optimization of highrise building structures. *Structural and Multidisciplinary Optimization*, *50*(6), 899–919.

Amezquita-Sanchez, J. P., Valtierra-Rodriguez, M., & Adeli, H. (2018). Wireless smart sensors for monitoring the health condition of civil infrastructure. *Scientia Iranica*, *25*(6), 2913–2925.

Bai, Z., Brunton, S. L., Brunton, B. W., Kutz, J. N., Kaiser, E., Spohn, A., & Noack, B. R. (2017). *Data-driven methods in fluid dynamics: Sparse classification from experimental data*. In A. Pollard, L. Castillo, L. Danaila, & M. Glauser (Eds.), *Whither turbulence and big data in the 21st century?* (pp. 323–342). Springer International Publishing.

Bastine, D., Vollmer, L., Wächter, M., & Peinke, J. (2018). Stochastic wake modelling based on POD analysis. *Energies*, *11*(3), 612.

Benito, N., Arias, J. R., Velazquez, A., & Vega, J. M. (2011). Real time performance improvement of engineering control units via higher order singular value decomposition: Application to a SI engine. *Control Engineering Practice*, *19*(11), 1315–1327.

Bernardini, E., Spence, S. M., Wei, D., & Kareem, A. (2015). Aerodynamic shape optimization of civil structures: A CFD-enabled Kriging-based approach. *Journal of Wind Engineering and Industrial Aerodynamics*, *144*, 154–164.

Bevanda, P., Sosnowski, S., & Hirche, S. (2021). Koopman operator dynamical models: Learning, analysis and control. *Annual Reviews in Control*, *52*, 197–212.

Błachowski, B., Świercz, A., Ostrowski, M., Tauzowski, P., Olaszek, P., & Jankowski, Ł. (2020). Convex relaxation for efficient sensor layout optimization in large-scale structures subjected to moving loads. *Computer-Aided Civil and Infrastructure Engineering*, *35*(10), 1085–1100.

Brunton, S. L., Brunton, B. W., Proctor, J. L., Kaiser, E., & Kutz, J. N. (2017). Chaos as an intermittently forced linear system. *Nature Communications*, *8*(1), 19..

Brunton, S. L., Proctor, J. L., Tu, J. H., & Kutz, J. N. (2016). Compressed sensing and dynamic mode decomposition. *Journal of Computational Dynamics*, *2*(2), 165–191.

Candès, E. J., Romberg, J. K., & Tao, T. (2006). Stable signal recovery from incomplete and inaccurate measurements. *Communications on Pure and Applied Mathematics*, *59*(8), 1207–1223.

Candes, E. J., & Wakin, M. B. (2008). An introduction to compressive sampling. *IEEE Signal Processing Magazine*, *25*(2), 21–30.

Carassale, L. (2012). Analysis of aerodynamic pressure measurements by dynamic coherent structures. *Probabilistic Engineering Mechanics*, *28*, 66–74.

Carassale, L., & Brunenghi, M. M. (2011). Statistical analysis of wind-induced pressure fields: A methodological perspective. *Journal of Wind Engineering and Industrial Aerodynamics*, *99*(6-7), 700–710.

Chen, X., & Kareem, A. (2004). Equivalent static wind loads on buildings: New model. *Journal of Structural Engineering*, *130*(10), 1425–1435.

Chen, X., & Kareem, A. (2005). Proper orthogonal decomposition-based modeling, analysis, and simulation of dynamic wind load effects on structures. *Journal of Engineering Mechanics*, *131*(4), 325–339.

Cui, W., & Caracoglia, L. (2018). A fully-coupled generalized model for multi-directional wind loads on tall buildings: A development of the quasi-steady theory. *Journal of Fluids and Structures*, *78*, 52–68.

Dawson, S. T., Hemati, M. S., Williams, M. O., & Rowley, C. W. (2016). Characterizing and correcting for the effect of sensor noise in the dynamic mode decomposition. *Experiments in Fluids*, *57*, 42.

Drmač, Z., & Gugercin, S. (2016). A new selection operator for the discrete empirical interpolation method—Improved a priori error bound and extensions. *SIAM Journal on Scientific Computing*, *38*(2), A631–A648.

Elshaer, A., Bitsuamlak, G., & El Damatty, A. (2017). Enhancing wind performance of tall buildings using corner aerodynamic optimization. *Engineering Structures*, *136*, 133–148.

Erichson, N. B., Mathelin, L., Yao, Z., Brunton, S. L., Mahoney, M. W., & Kutz, J. N. (2020). Shallow neural networks for fluid flow reconstruction with limited sensors. *Proceedings of the Royal Society A*, *476*(2238), 20200097.

Frame, P., & Towne, A. (2023). Space-time POD and the Hankel matrix. *PLoS ONE*, *18*(8), e0289637.

Fu, Y., Lin, X., Li, L., Chu, Q., Liu, H., Zheng, X., Liu, C. H., Chen, Z., Lin, C., Tse, T. K. T., & Li, C. Y. (2023). A POD-DMD augmented procedure to isolating dominant flow field features in a street canyon. *Physics of Fluids*, *35*(2), 025112.

Gao, H., Hu, G., Zhang, D., Jiang, W., Tse, K. T., Kwok, K. C. S., & Kareem, A. (2024). Urban wind field prediction based on sparse sensors and physics-informed graph-assisted autoencoder. *Computer-Aided Civil and Infrastructure Engineering*, *39*(10), 1409–1430.

Gao, H., Liu, J., Lin, P., Hu, G., Patruno, L., Xiao, Y., Tse, K. T., & Kwok, K. C. S. (2023). An optimal sensor placement scheme for wind flow and pressure field monitoring. *Building and Environment*, *244*, 110803.

Gutierrez Soto, M., & Adeli, H. (2017). Many-objective control optimization of high-rise building structures using replicator dynamics and neural dynamics model. *Structural and Multidisciplinary Optimization*, *56*(6), 1521–1537.

Haar, A. (1910). Zur Theorie der orthogonalen Funktionensysteme: Erste Mitteilung. *Mathematische Annalen*, *69*(3), 331–371.

Hemati, M. S., Rowley, C. W., Deem, E. A., & Cattafesta, L. N. (2017). De-biasing the dynamic mode decomposition for applied Koopman spectral analysis of noisy datasets. *Theoretical and Computational Fluid Dynamics*, *31*, 349–368.

Higham, N. J. (2000). QR factorization with complete pivoting and accurate computation of the SVD. *Linear Algebra and its Applications*, *309*(1), 153–174.

Hu, G., Song, J., Hassanli, S., Ong, R., & Kwok, K. C. (2019). The effects of a double-skin façade on the cladding pressure around a tall building. *Journal of Wind Engineering and Industrial Aerodynamics*, *191*, 239–251.

Huang, G., & Chen, X. (2007). Wind load effects and equivalent static wind loads of tall buildings based on synchronous pressure measurements. *Engineering Structures*, *29*(10), 2641–2653.

Hwang, J. S., Kwon, D. K., & Kareem, A. (2023). A modal-based Kalman filtering framework for mode extraction and decomposition of damped structures. *Computer-Aided Civil and Infrastructure Engineering*, *38*(10), 1274–1289.

Jiang, X., & Adeli, H. (2007). Pseudospectra, MUSIC, and dynamic wavelet neural network for damage detection of highrise buildings. *International Journal for Numerical Methods in Engineering*, *71*(5), 606–629.

Jolliffe, I. T., & Cadima, J. (2016). Principal component analysis: A review and recent developments. *Philosophical Transactions of the Royal Society A: Mathematical, Physical and Engineering Sciences*, *374*(2065), 20150202.

Joshi, S., & Boyd, S. (2009). Sensor selection via convex optimization. *IEEE Transactions on Signal Processing*, *57*(2), 451–462.

Karnik, N., Abdo, M. G., Estrada-Perez, C. E., Yoo, J. S., Cogliati, J. J., Skifton, R. S., Calderoni, P., Brunton, S. L., & Manohar, K. (2024). Constrained optimization of sensor placement for nuclear digital twins. *IEEE Sensors Journal*, *24*(9), 15501–15516.

Kim, H., & Adeli, H. (2005). Wind-induced motion control of 76-story benchmark building using the hybrid damper-tlcd system. *Journal of Structural Engineering*, *131*(12), 1794–1802.

Kociecki, M., & Adeli, H. (2014). Two-phase genetic algorithm for topology optimization of free-form steel space-frame roof structures with complex curvatures. *Engineering Applications of Artificial Intelligence*, *32*, 218–227.

Kutz, J. N., Fu, X., & Brunton, S. L. (2016). Multiresolution dynamic mode decomposition. *SIAM Journal on Applied Dynamical Systems*, *15*(2), 713–735.

Lange, H., Brunton, S. L., & Kutz, J. N. (2021). From Fourier to Koopman: Spectral methods for long-term time series prediction. *Journal of Machine Learning Research*, *22*(41), 1–38.

Li, C. Y., Chen, Z., Tse, T. K., Weerasuriya, A. U., Zhang, X., Fu, Y., & Lin, X. (2022). A parametric and feasibility study for data sampling of the dynamic mode decomposition: Spectral insights and further explorations. *Physics of Fluids*, *34*(3), 035102.

Li, C. Y., Chen, Z., Weerasuriya, A. U., Zhang, X., Lin, X., Zhou, L., & Tim, K. T. (2023). Best practice guidelines for the dynamic mode decomposition from a wind engineering perspective. *Journal of Wind Engineering and Industrial Aerodynamics*, *241*, 105506.

Li, S., Snaiki, R., & Wu, T. (2021). A knowledge-enhanced deep reinforcement learning-based shape optimizer for aerodynamic mitigation of wind-sensitive structures. *Computer-Aided Civil and Infrastructure Engineering*, *36*(6), 733–746.

Li, Z., Park, H. S., & Adeli, H. (2017). New method for modal identification of super high-rise building structures using discretized synchrosqueezed wavelet and Hilbert transforms. *Structural Design of Tall and Special Buildings*, *26*(3), e1312.

Lindeberg, T. (2015). Image matching using generalized scale-space interest points. *Journal of Mathematical Imaging and Vision*, *52*(1), 3–36.

Liu, W., Gao, W., Sun, Y., & Xu, M. (2008). Optimal sensor placement for spatial lattice structure based on genetic algorithms. *Journal of Sound and Vibration*, *317*(1–2), 175–189.

Luo, X., & Kareem, A. (2021). Dynamic mode decomposition of random pressure fields over bluff bodies. *Journal of Engineering Mechanics*, *147*(4), 04021007.

Ma, Y., Zheng, Y. B., Wang, S. Y., Wong, Y. D., & Easa, S. M. (2023). Virtual-real-fusion simulation framework for evaluating and optimizing small-spatial-scale placement of cooperative roadside sensing units. *Computer-Aided Civil and Infrastructure Engineering*, *39*(5), 707–730.

Manohar, K., Brunton, B. W., Kutz, J. N., & Brunton, S. L. (2018). Data-driven sparse sensor placement for reconstruction: Demonstrating the benefits of exploiting known patterns. *IEEE Control Systems Magazine*, *38*(3), 63–86.

Manohar, K., Kaiser, E., Brunton, S. L., & Kutz, J. N. (2019). Optimized sampling for multiscale dynamics. *Multiscale Modeling & Simulation*, *17*(1), 117–136.

Manohar, K., Kutz, J. N., & Brunton, S. L. (2022). Optimal sensor and actuator selection using balanced model reduction. *IEEE Transactions on Automatic Control*, *67*(4), 2108–2115.

Meena, R. K., Raj, R., & Anbukumar, S. (2022). Wind excited action around tall building having different corner configurations. *Advances in Civil Engineering*, *2022*, 1–17.

Meo, M., & Zumpano, G. (2005). On the optimal sensor placement techniques for a bridge structure. *Engineering Structures*, *27*(10), 1488–1497.

Muld, T. W., Efraimsson, G., & Henningson, D. S. (2012). Flow structures around a high-speed train extracted using Proper OrthogonalDecomposition and Dynamic Mode Decomposition. *Computers & Fluids*, *57*, 87–97.

Nair, A. G., & Taira, K. (2015). Network-theoretic approach to sparsified discrete vortex dynamics. *Journal of Fluid Mechanics*, *768*, 549–571.

Papadimitriou, C. (2004). Optimal sensor placement methodology for parametric identification of structural systems. *Journal of Sound and Vibration*, *278*(4-5), 923–947.

Park, H. S., & Adeli, H. (1997). Data parallel neural dynamics model for integrated design of large steel structures. *Computer-Aided Civil and Infrastructure Engineering*, *12*(5), 311–326.

Peherstorfer, B., Drmač, Z., & Gugercin, S. (2020). Stability of discrete empirical interpolation and gappy proper orthogonal decomposition with randomized and deterministic sampling points. *SIAM Journal on Scientific Computing*, *42*(5), A2837–A2864.

Perez-Ramirez, C. A., Amezquita-Sanchez, J. P., Adeli, H., Valtierra-Rodriguez, M., Camarena-Martinez, D., & Romero-Troncoso, R. R. J. (2016). New methodology for modal parameters identification of smart civil structures using ambient vibrations and synchrosqueezed wavelet. *Engineering Applications of Artificial Intelligence*, *48*, 1–16.

Rowley, C. W., Mezić, I., Bagheri, S., Schlatter, P., & Henningson, D. S. (2009). Spectral analysis of nonlinear flows. *Journal of Fluid Mechanics*, *641*, 115–127.

Schmid, P. J. (2010). Dynamic mode decomposition of numerical and experimental data. *Journal of Fluid Mechanics*, *656*, 5–28.

Sharma, A., Mittal, H., & Gairola, A. (2018). Mitigation of wind load on tall buildings through aerodynamic modifications. *Journal of Building Engineering*, *18*, 180–194.

Takens, F. (1981). Detecting strange attractors in turbulence. In D. Rand & L.-S. Young (Eds.), *Lecture notes in mathematics: Vol 898. Dynamical systems and turbulence, Warwick 1980* (pp. 366–381). Springer.

Tamura, Y., Suganuma, S., Kikuchi, H., & Hibi, K. (1999). Proper orthogonal decomposition of random wind pressure field. *Journal of Fluids and Structures*, *13*(7-8), 1069–1095.

Tan, Y., & Zhang, L. (2020). Computational methodologies for optimal sensor placement in structural health monitoring: A review. *Structural Health Monitoring*, *19*(4), 1287–1308.

Tanaka, H., Tamura, Y., Ohtake, K., Nakai, M., & Kim, Y. C. (2012). Experimental investigation of aerodynamic forces and wind pressures acting on tall buildings with various unconventional configurations. *Journal of Wind Engineering and Industrial Aerodynamics*, *107*, 179–191.

Tse, K. T., Hitchcock, P. A., Kwok, K. C., Thepmongkorn, S., & Chan, C. M. (2009). Economic perspectives of aerodynamic treatments of square tall buildings. *Journal of Wind Engineering and Industrial Aerodynamics*, *97*(9-10), 455–467.

Tu, J. H., Rowley, C. W., Kutz, J. N., & Shang, J. K. (2014). Spectral analysis of fluid flows using sub-Nyquist-rate PIV data. *Experiments in Fluids*, *55*, 1–13.

Van Beers, W. C. M., & Kleijnen, J. P. C. (2004). Kriging interpolation in simulation: A survey. *Proceedings of the 2004 Winter Simulation Conference, 2004*. Washington, DC (pp. 107–115).

Wang, N., & Adeli, H. (2015). Robust vibration control of wind-excited highrise building structures. *Journal of Civil Engineering and Management*, *21*(8), 967–976.

Waqas, U. A., Khan, M., & Batool, S. I. (2020). A new watermarking scheme based on Daubechies wavelet and chaotic map for quick response code images. *Multimedia Tools and Applications*, *79*(9), 6891–6914.

Whiteman, M. L., Fernández-Cabán, P. L., Phillips, B. M., Masters, F. J., Davis, J. R., & Bridge, J. A. (2022). Cyber-physical aerodynamic shape optimization of a tall building in a wind tunnel using an active fin system. *Journal of Wind Engineering and Industrial Aerodynamics*, *220*, 104835.

Wijesooriya, K., Mohotti, D., Lee, C. K., & Mendis, P. (2023). A technical review of computational fluid dynamics (CFD) applications on wind design of tall buildings and structures: Past, present and future. *Journal of Building Engineering*, *74*, 106828.

Xie, X., Cai, J., Wang, H., Wang, Q., Xu, J., Zhou, Y., & Zhou, B. (2022). Sparse-sensing and superpixel-based segmentation model for concrete cracks. *Computer-Aided Civil and Infrastructure Engineering*, *37*(13), 1769–1784.

Yang, C. (2021). An adaptive sensor placement algorithm for structural health monitoring based on multi-objective iterative optimization using weight factor updating. *Mechanical Systems and Signal Processing*, *151*, 107363.

Yao, L., Sethares, W. A., & Kammer, D. C. (1993). Sensor placement for on-orbit modal identification via a genetic algorithm. *AIAA Journal*, *31*(10), 1922–1928.

Yi, T. H., Li, H. N., & Gu, M. (2011). Optimal sensor placement for structural health monitoring based on multiple optimization strategies. *Structural Design of Tall and Special Buildings*, *20*(7), 881–900.

Yuan, Y., Au, F. T., Yang, D., & Zhang, J. (2023). Active learning structural model updating of a multisensory system based on Kriging method and Bayesian inference. *Computer-Aided Civil and Infrastructure Engineering*, *38*(3), 353–371.

Zhang, Q., Liu, Y., & Wang, S. (2014). The identification of coherent structures using proper orthogonal decomposition and dynamic mode decomposition. *Journal of Fluids and Structures*, *49*, 53–72.

Zhao, Y., Zhao, M., Li, X., Liu, Z., & Du, J. (2019). A modified proper orthogonal decomposition method for flow dynamic analysis. *Computers & Fluids*, *182*, 28–36.

Zhou, L., Tse, K. T., Hu, G., & Li, Y. (2021). Higher order dynamic mode decomposition of wind pressures on square buildings. *Journal of Wind Engineering and Industrial Aerodynamics*, *211*, 104545.

How to cite this article: Snaiki, R., & Mirfakhar, S. F. (2024). Multiresolution dynamic mode decomposition approach for wind pressure analysis and reconstruction around buildings. *Computer-Aided Civil and Infrastructure Engineering*, 1–17. https://doi.org/10.1111/mice.13304